J. Biomed. Eng. Res.
Vol. 23, No. 4, 269-279, 2002

3차원 자기공명 전류밀도 영상법의 수치적 해석

이병일[1] · 오석훈[2] · 우응제[1] · 강곤[1] · 이수열[2] · 조민형[2] · 권오인[3] · 윤정록[4] · 서진근[5]

[1]경희대학교 전자정보학부 동서의료공학과, [2]경희대학교 동서의학대학원 [3]건국대학교 수학과,
[4]고등과학원 수학부, [5]연세대학교 수학과

(2002년 4월 22일 접수, 2002년 8월 21일 채택)

Numerical Analysis of Three-Dimensional Magnetic Resonance Current Density Imaging (MRCDI)

B.I. Lee[1], S.H. Oh[2], E.J. Woo[1], G. Khang[1], S.Y. Lee[2], M.H. Cho[2], O. Kwon[3], J-R. Yoon[4], J.K. Seo[5]

[1]College of Electronics and Information, Kyung Hee University, Korea [2]Graduate School of East-West Medical Sciences, Kyung Hee University, Korea [3]Department of Mathematics, Konkuk University, Korea [4]School of Mathematics, Korea Institute for Advanced Study, Korea [5]Department of Mathematics, Yonsei University, Korea

(Received April 22, 2002. Accepted August 21, 2002)

요 약 : 인체에 전류주입하면, 내부에는 전압 및 전류밀도의 분포가 형성된다. 이때, 인체내부의 전류밀도와 전류를 주입하는 도선에 흐르는 전류는 자장을 형성하게 된다. 인체내부에 유기된 자속밀도는 자기공명영상의 위상을 변화시키므로, 위상영상으로부터 자속밀도를 측정할 수 있다. 자속밀도의 curl을 취하여 전류밀도를 구하면, 주입전류에 의한 내부의 전류밀도 분포를 영상화하는 것이 가능하다. 이러한 자기공명 전류밀도 영상법을 자기공명 임피던스 단층촬영에 응용하여 고해상도의 저항률 영상을 복원하는 연구가 진행되고 있다. 본 논문에서는 인체와 같은 전도성 물체에 전류를 주입할 때, 내부에 형성되는 전압, 전류밀도 및 자속밀도의 3차원적인 분포를 수치적으로 계산하는 방법을 기술한다. 이러한 수치적인 해석기술은 자기공명 전류밀도 영상법의 실험방법 설계와 자기공명 임피던스 단층촬영의 영상복원 알고리즘 개발에 필수적인 부분이다. 본 논문에서는 유한요소법과 Biot-Savart 법칙에 기반하여, 여러가지 모델에서 계산한 결과를 기술하고, 그 해석을 통하여 수치적인 해의 정확도와 유의성을 검증하였다.

Abstract : When we inject a current into an electrically conducting subject such as a human body, voltage and current density distributions are formed inside the subject. The current density within the subject and injection current in the lead wires generate a magnetic field. This magnetic flux density within the subject distorts phase of spin-echo magnetic resonance images. In Magnetic Resonance Current Density Imaging (MRCDI) technique, we obtain internal magnetic flux density images and produce current density images from $J=\nabla\times B/\mu_0$. This internal information is used in Magnetic Resonance Electrical Impedance Tomography (MREIT) where we try to reconstruct a cross-sectional resistivity image of a subject. This paper describes numerical techniques of computing voltage, current density, and magnetic flux density within a subject due to an injection current. We use the Finite Element Method (FEM) and Biot-Savart law to calculate these variables from three-dimensional models with different internal resistivity distributions. The numerical analysis techniques described in this paper are used in the design of MRCDI experiments and also image reconstruction algorithms for MREIT.

Key words : MRCDI, MREIT, Injection current, Current density, Magnetic flux density, FEM, Biot-Savart law

INTRODUCTION

In Magnetic Resonance Current Density Imaging (MRCDI), we inject a current into an electrically conducting subject such as a human body to quantitatively visualize internal current density distributions [1] -[5]. Injection currents through surface electrodes produce voltage and current density distributions within the subject. The current density

본 연구는 2001년도 경희대학교의 지원으로 수행되었음.
통신저자 : 강 곤, (449-701) 경기도 용인시 기흥읍 서천리 1
경희대학교 전자정보학부
Tel. (031)201-2998, Fax. (031)205-9062
E-mail. gkhang@khu.ac.kr

inside the subject and lead wires induces a magnetic field. We can measure the magnetic flux density within the subject from MR phase images since this magnetic field due to injection currents generates additional phase changes. MRCDI has finding many applications where we need to inspect internal current density distributions especially in electrical stimulation of biological tissues[6, 7].

Lately, Magnetic Resonance Electrical Impedance Tomography (MREIT) has been suggested to reconstruct cross-sectional resistivity images of a subject [8]-[13] by incorporating the conventional Electrical Impedance Tomography (EIT) with MRCDI technique. MREIT is very promising to reconstruct accurate cross-sectional resistivity images with a high spatial resolution since it enables us to utilize the internal magnetic flux and/or current density distribution due to an injection current. Most reconstruction algorithms in MREIT require a forward solver computing internal current density and/or magnetic flux density distributions due to an injection current. *Lee et al.* recently developed a three-dimensional forward solver for MREIT using the finite element method (FEM) and Biot-Savart law[14].

In this paper, we focus our attention on the numerical analysis of MRCDI technique to design experimental procedures and find the required performance of the MRCDI system. After we define the MRCDI problem, we will describe the numerical techniques adopted in this paper. It is a volume conductor problem where we must consider distributions of voltage, current density, and also magnetic flux density within an electrically conducting subject. In addition, we must also include the lead wires attached to electrodes on the surface of the subject in computing the magnetic flux density.

METHODS

A. MRCDI Problem Definition

Let $\Omega \subset \mathrm{IR}^3$ be an electrically conducting subject with its boundary denoted by $\partial\Omega$ as shown in Fig. 1. In this paper, we model the subject as a cubic body only for simplicity. A position vector in IR^3 is denoted as $r = (x, y, z)$. When we inject a current I through electrodes *E1* and *E2* attached on $\partial\Omega$, we can formulate the following elliptic partial differential equation:

$$\nabla\left[\frac{1}{\rho(r)}\nabla V(r)\right] = 0 \text{ in } \Omega \tag{1}$$

$$\text{with } \frac{1}{\rho}\frac{\partial V}{\partial n} = J \text{ on } \partial\Omega, \quad \int_{\partial\Omega} V ds = 0, \text{ and } \int_{\partial\Omega} J ds = 0$$

where $\rho(r)$ and $V(r)$ are resistivity and voltage distribution in Ω, respectively, n is the outward unit normal vector on $\partial\Omega$, and J is a magnitude of current density due to the injection current I. Once we have found a numerical solution $V(r)$ of (1), we can compute the internal current density distribution due to the injection current I *as*

$$J(r) = -\frac{1}{\rho(r)}\nabla V(r) \tag{2}$$

Now, we denote the magnetic flux density at $r \in \Omega$ as $B(r)$. As shown in Fig. 1, we consider two lead wires carrying the injection current I from the infinity to electrodes *E1* and *E2*. For the purpose of numerical computations, we divide into three components as

$$B(r) = B_J(r) + B_{I^+}(r) + B_{I^-}(r) \tag{3}$$

where $B_J(r)$ and $B_{I^\pm}(r)$ are magnetic flux densities due to J in Ω and I of the two lead wires in $\mathrm{IR}\backslash\Omega$, respectively. From the Biot-Savart law [15, 16], we have

$$B_J(r) = \frac{\mu_0}{4\pi}\int_\Omega J(r') \times \frac{r - r'}{|r - r'|^3} dv', \tag{4}$$

$$B_{I^+}(r) = \frac{\mu_0}{4\pi}\int_{L^+} I(r')a(r') \times \frac{r - r'}{|r - r'|^3} dl', \tag{5}$$

$$B_{I^-}(r) = \frac{\mu_0}{4\pi}\int_{L^-} I(r')a(r') \times \frac{r - r'}{|r - r'|^3} dl', \tag{6}$$

where is μ_0 the permeability of free space and biological tissues, $L^\pm$ are regions of the lead wires in $\mathrm{IR}^3\backslash\Omega$, and $a(r')$is the unit vector in the direction of the lead wire at $r' \in L^\pm$.

After we compute $B(r)$, it must satisfy the following equation:

$$J^B(r) = \frac{1}{\mu_0}\nabla \times B(r) \text{ in } \Omega \tag{7}$$

In MRCDI experiments, we compute $J^B(r)$ using (7) from the measured $B(r)$ [13]. In this paper, we use (7) for the numerical error analysis of computational results

since $J(r)$ in (2) and $J^B(r)$ in (7) must be the same. For the compatibility of the solutions $J(r)$ and $J^B(r)$, we also verify if

$$\nabla \cdot J(r) = 0 \text{ and } \nabla \cdot J^B(r) = 0 \text{ in } \Omega \tag{8}$$

are satisfied.

B. Numerical Solutions V(r) of and J(r)

In numerically solving (1), FEM can accommodate Ω with arbitrary shape and $\rho(r)$. However, in this paper, we use the cubic model ($2L \times 2L \times 2L$) with isotropic $\rho(r)$ shown in Fig. 1 for simplicity. For the discretization of the model into a finite element mesh, we use eight-node hexahedral elements. Using the Galerkin method [16, 17], we evaluate the 8×8 element matrix for each element. For a mesh with N nodes and E elements, we compute element matrices for all elements and assemble the $N \times N$ master matrix $\boldsymbol{Y}$ in such a way we preserve the inter-elements continuity of nodal voltage values. Then, we can formulate the following linear system of equations providing an approximate numerical solution of (1).

$$Yv = c \tag{9}$$

where v is a $N \times 1$ node voltage vector and c is a $N \times 1$ node current vector including the Neumann boundary condition in (1). Lee *et al.* describes the details in using FEM for the numerical solution of (1) [14]. After we compute all nodal voltages from (9), we can easily compute the current density $J(r)$ in (2) for each element.

C. Numerical Solutions of B(r) and $J^B(r)$

We compute the magnetic flux density $B(r)$ in (3) using (4)-(6). Assuming that the current density within the e-th element does not change much for each element in the mesh, we compute $B_J(r)$ with $r \in \Omega$ in (4) as

$$B_J(r) = \frac{\mu_0}{4\pi} \sum_{e=1}^{E} J_c^{(e)} \times \frac{r - r_c^{(e)}}{|r - r_c^{(e)}|^3} \triangle v^{(e)} \tag{10}$$

where $r_c^{(e)}$ is the center point of the e-th element, $J_c^{(e)}$ is the current density at $r_c^{(e)}$, and $\triangle v^{(e)}$ is the volume of the element. In order to avoid the singularity where the field point r is equal to the source point $r_c^{(e)}$, we let r be all nodal points of the mesh.

To compute $B_{I^1}(r)$ with $r = (x, y, z) \in \Omega$ in (5) and (6), we consider three different methods including analytic formula, single-line FEM, and multi-line FEM method. In the analytic formula method, we use the following formula [18]:

$$B_I^{AF}(x, y, z) = B_{I^+}(x, y, z) + B_{I^-}(x, y, z)$$
$$= \frac{\mu_0}{4\pi} \frac{(Z, 0, -x}{x^2 + z^2} \left\{ 2 - \frac{\mathrm{L} - \mathrm{y}}{\sqrt{(\mathrm{L}-\mathrm{y})^2 + \mathrm{x}^2 + \mathrm{z}^2}} - \frac{\mathrm{L} + \mathrm{y}}{\sqrt{(\mathrm{L}-\mathrm{y})^2 + \mathrm{x}^2 + \mathrm{z}^2}} \right\} \tag{11}$$

excluding two nodal points of $r = (0, \pm L, 0)$ where two lead wires are connected to the cubic model. In the single-line FEM method, we divide the regions $L^{\pm}$ of two lead wires into L line segments. We limit the length of $L^{\pm}$ to ten times the dimension of Ω, that is, $20L$ since the contribution from a line segment is inversely proportional to the square of the distance between the field and source point. Then, for $r = (x, y, z) \in \Omega$,

$$\mathrm{B}_{\mathrm{I}^{\pm}}^{\mathrm{SL}}(\mathrm{r}) = \mathrm{B}_{\mathrm{I}^{+}} + \mathrm{B}_{\mathrm{I}^{-}} = \frac{\mu_0}{4\pi} \sum_{l=1}^{L} \mathrm{Ia}_y \times \frac{|\mathrm{r} - \mathrm{r}_c^{(l)}|}{|\mathrm{r} - \mathrm{r}_c^{(l)}|^3} \triangle \ell \tag{12}$$

where $r_c^{(l)}$ is the center point and $\triangle l$ is the length of the l-th line segment, respectively.

To describe the multi-line FEM method, we first define two sets of nodal points $\Psi_1 = \{\text{all nodal points under } E_1\}$ and $\Psi_2 = \{\text{all nodal points under } E_2\}$. For each nodal point in Ψ_1 and Ψ_2, we assume that a lead wire with the length of $20L$ is attached. We assign the amount of current in each lead wire as the value of the current in the corresponding element of c in (9). Then, for $r = (x, y, z) \in \Omega$,

$$B_{I^{\pm}}^{ML}(r) = \mathrm{B}_{\mathrm{I}^{+}} + \mathrm{B}_{\mathrm{I}^{-}} = \frac{\mu_0}{4\pi} \sum_{w=1}^{W} \sum_{l=1}^{L} c_w a_y \times \frac{r - r_c^{(w,l)}}{|r - r_c^{(w,l)}|^3} \triangle l \tag{13}$$

where W is the total number of nodal points in Ψ_1 and Ψ_2, c_w is the amount of the distributed injection current at the w-th node in Ψ_1 and Ψ_2, and $r_c^{(w,l)}$ is the center point of the l-th line segment connected to the w-th node. Note that $\sum_{w=1}^{W} c_w = I$. Since we compute the magnetic flux density $B(r)$ on all nodal points in Ω, we can easily calculate $J^B(r)$ in (7).

Before we present numerical results, we note that different lead wire geometries produce different results of

$B(r)$ in Ω as expressed in (5) and (6). However, Lee *et al.* showed that the difference in $B(r)$ due to changes in lead wire geometry is a curl and divergence free vector [14]. They also showed that $J^B(r)$ in (7) is only dependent on the Neumann boundary condition in (1). This means that the implication of different lead wire geometry affects the computation of only $B(r)$ not $J^B(r)$. Therefore, the simplest lead wire geometry in Fig. 1 is sufficient for the computation of $J^B(r)$ even though the actual shape of each lead wire is very different from the straight line. We discussed the effects of lead wire geometry on the measured $B(r)$ in [19]. We also showed that the error in $B(r)$ due to different lead wire geometry could be appropriately handled in MREIT image reconstruction problems in [14].

Three methods in (10), (11), and (12) produce the same Neumann boundary condition in (1) and this means that we should get the same $J^B(r)$ in theory. However, they treat the singularity problem near electrode where the denominators in (5) and (6) become very small or zero. This requires us to check whether the compatibility conditions in the numerical results of $J^B(r)$ are satisfied.

D. Numerical Implementation

Fig. 2 shows three different models (300×300×300 mm) used in this paper. The models are equipped with two long surface electrodes (9.4×300 mm). The first model in Fig. 2(a) is homogeneous with $\rho(r)=\rho_0=300$ Ωcm for any $r\in\Omega$. The second model in Fig. 2(b) contains two cylindrical anomalies of 30 and 3,000 Ωcm resistivity. The third model in Fig. 2(c) mimics the human thorax including two lungs (1,000 Ωcm), heart (50 Ωcm), and spine (10,000 Ωcm). For each model, the corresponding finite element mesh contains 64×64×35 elements (total 143,360 elements) and 152,100 nodes. Lee *at al.* showed that the chosen mesh provides enough numerical accuracy for applications in MRCDI and MREIT[14].

In obtaining numerical results described in the following section, we set the injection current as 55 mA. For each numerical result, we performed two compatibility tests. One is to check if two current density distributions in (2) and (7) are the same. The other is the agreement with the continuity equations in (8). We performed all computations using a PC (Precision 530MT, Dell Computer Co., USA) with dual 1.7 GHz Xeon processors, 256 KB L2 cache, 1 GB of RDRAM, 18 GB of SCSI hard disk, and Windows 2000 Professional operating system. We used double precision floating point variables for all calculations.

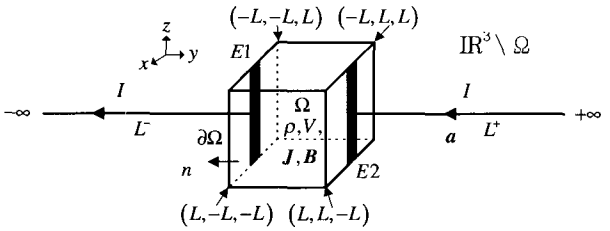

Fig. 1. An electrically conducting body $\Omega\subset\mathbb{R}^3$ with its resistivity distribution ρ. Two highly conductive electrodes E_1 and E_2 are placed on its boundary $\partial\Omega$ and we inject a current I between E_1 and E_2 via two lead wires.

RESULTS

A. Homogeneous Model

In this section, we describe the numerical results of three different methods in computing the magnetic flux density in (11), (12), and (13) using the homogeneous model in Fig. 2(a). Fig. 3(a) and (b) show the computed B_z and $|J^B|$, respectively, on the xy-plane with z=0 mm using the analytic formula method in (11). In Fig. 3(b), the current density near electrodes are over estimated resulting in a large difference between J and J^B. We also found that $\nabla\cdot J^B$ is much greater than zero near elect-

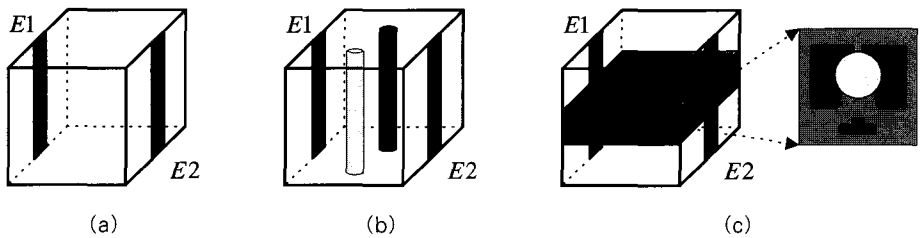

Fig. 2. Three models used in numerical analyses of MRCDI. (a) Homogeneous model of 300 Ωcm. (b) Inhomogeneous model with two cylindrical anomalies of 30 and 3,000 Ωcm. (c) Thorax model with two lungs (1,000 Ωcm), heart (50 Ωcm), and spine (10,000 Ωcm).

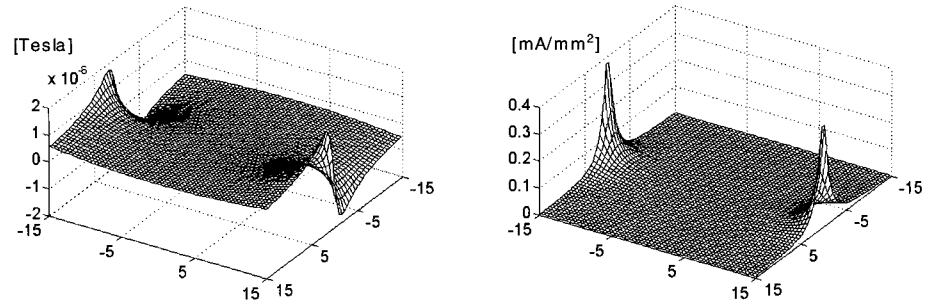

Fig. 3. Computed (a) B_z and (b) $|J^B|$ on the xy-plane with $z = 0$ mm in Ω for the homogeneous model shown in Fig. 2(a) using the analytic formula method.

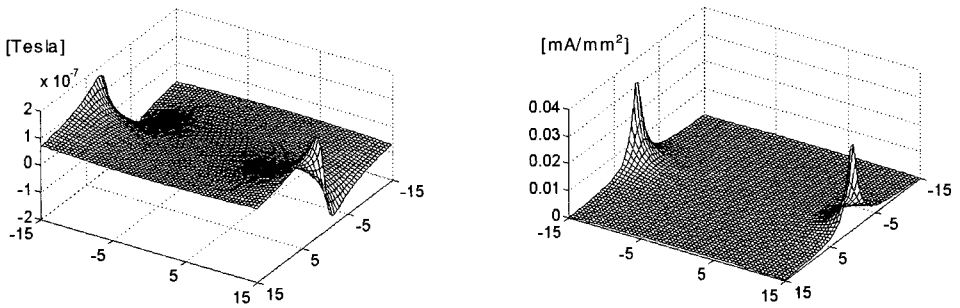

Fig. 4. Computed (a) B_z and (b) $|J^B|$ on the xy-plane with z = 0 mm in Ω for the homogeneous model shown in Fig. 2(a) using the Single-line method.

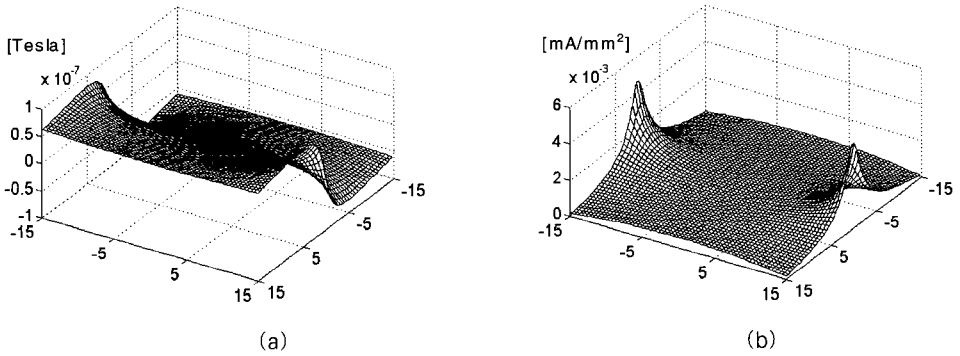

Fig. 5. Computed (a) B_z and (b) $|J^B|$ on the xy-plane with z = 0 mm in Ω for the homogeneous model shown in Fig. 2(a) using the multi-line method.

rodes due to the singularity at the interface between electrodes and lead wires.

Fig. 4(a) and (b) show the computed B_z and $|J^B|$, respectively, on the xy-plane with $z = 0$mm using the single-line method in (12). We could also find that the single-line method fails to treat the singularity problem appropriately from a large difference between J and J^B and nonzero $\nabla \cdot J^B$ near electrodes.

Fig. 5(a) and (b) show the computed B_z and $|J^B|$, respectively, on the xy-plane with $z = 0$ mm using the multi-line method in (13). Erroneously overestimated peaks near electrodes in Fig. 3 and 4 are now replaced by peaks

with correct amplitudes in Fig. 5. This implies that the multi-line method effectively avoids the singularity problem near electrodes. We could find a negligibly small root-mean-squared (rms) error between J and J^B. Two compatibility conditions in (8) are also satisfied with negligibly small rms errors (10^{-8}or 10^{-7} mA/mm^2). Therefore, we

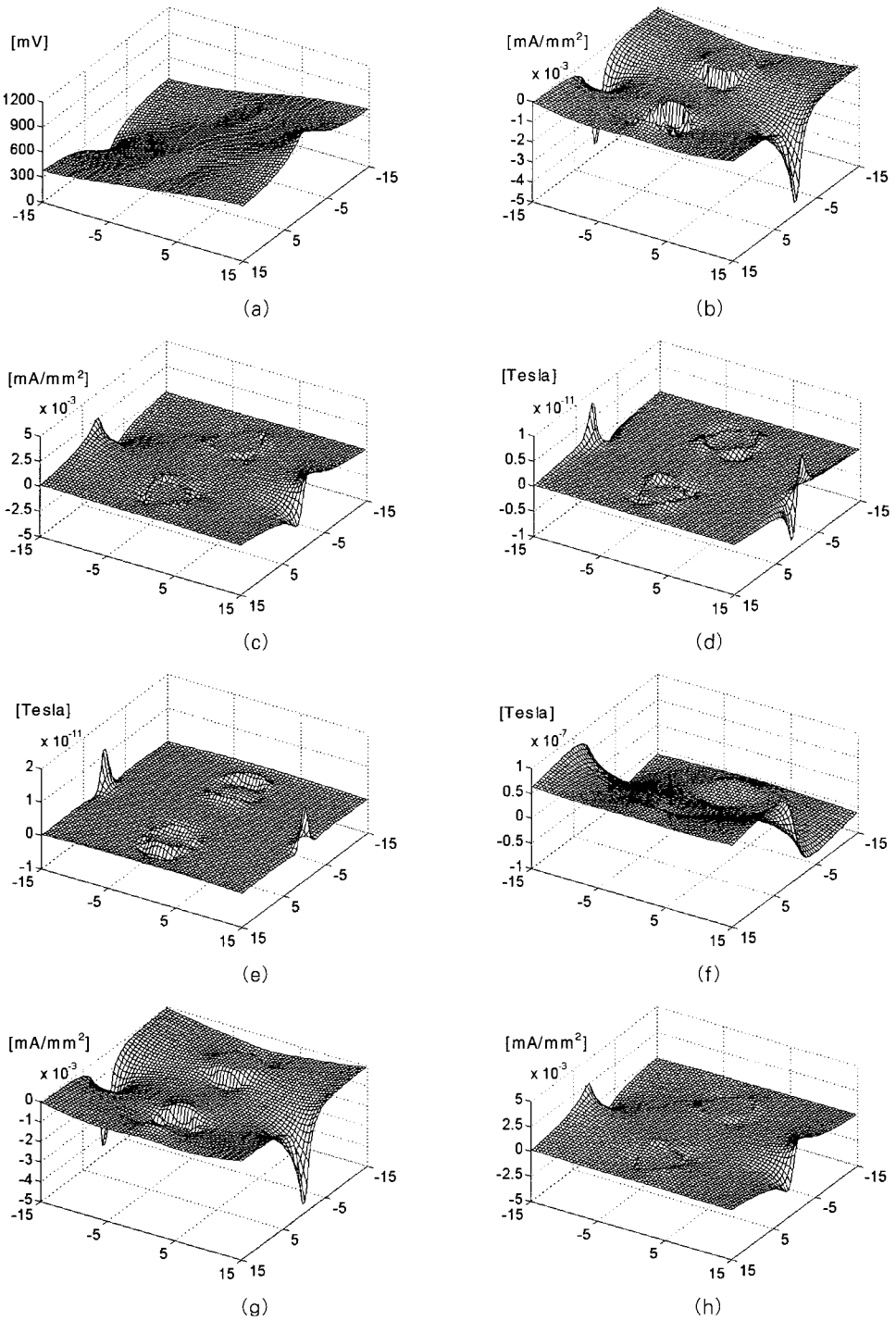

Fig. 6. Computed (a) V, (b) J_x, and (c) J_y on the xy-plane with z = 0 mm in Ω for the model with two cylindrical anomalies shown in Fig. 2(b). Computed (d) B_x, (e) B_y, (f) B_y, (g) J_x^B, and (h) J_y^B on the same plane for the same model.

choose the multi-line method in computing $B(r)$ in the remaining parts of this paper.

B. Inhomogeneous Model with Two Cylindrical Anomalies

Fig. 6(a) shows the computed voltage on the xy-plane with $z = 0$ mm in Ω for the model in Fig. 2(b). Fig. 6(b) and (c) show the computed J_x and J_y, respectively. The computed value of J_z was negligibly small ($\sim 10^{-17}$ mA/mm^2). Fig. 6(d), (e), and (f) show the computed B_x, B_y, and B_z, respectively. Since there is no change in resistivity distribution along z-direction and we computed B on the middle plane ($z = 0$ mm), B_x and B_y are much smaller than B_z. Fig. 6(g) and (h) show the computed J_x^B and J_y^B, respectively. The computed value of J_z^B was negligibly small ($\sim 10^{-6}$ mA/mm^2). We found that the compatibility condition of $J(r)=J^B(r)$ and continuity equations of $\nabla \cdot J(r)=0$ and $\nabla \cdot J^B(r)=0$ are all satisfied with negligibly small values of rms errors (10^{-5} or 10^{-6}).

C. Thorax Model

Fig. 7(a) shows the resistivity distribution of the thorax model in Fig. 2(c) on the xy-plane with $z = 0$ mm in Ω. Fig. 7(b) is the computed voltage on the same plane. Fig. 7(c) and (d) show the computed J_x and J_y, respectively. The computed value of J_z was negligibly small ($\sim 10^{-17}$ mA/mm^2) since the resistivity distribution is symmetric with respect to the plane along z-direction. Fig. 8(a), (b), and (c) show the computed B_x, B_y, and B_z, respectively. Since we computed B on the middle plane ($z = 0$ mm), and are much smaller than B_z. Fig. 8(d) and (e) show the computed J_x^B and J_y^B, respectively. The computed value of J_z^B was negligibly small ($\sim 10^{-6}$ mA/mm^2). Fig. 8(f) shows the vector plot of the current density J^Bin the same xy-plane. We found that the compatibility condition of $J(r)=J^B(r)$ and continuity equations of $\nabla \cdot J(r)=0$ and $\nabla \cdot J^B(r)=0$ are all satisfied with negligibly small values of rms errors.

Fig. 9 (a) shows the computed voltage on the xy-plane with $z = 42.85$ mm in Ω. Fig. 9(b), (c), and (d) are computed B_x, B_y, and B_z on the same plane. We can see that B_x and B_y on this plane are much larger than B_x and B_y on the xy-plane with $z = 0$ mm. This implies that B_x

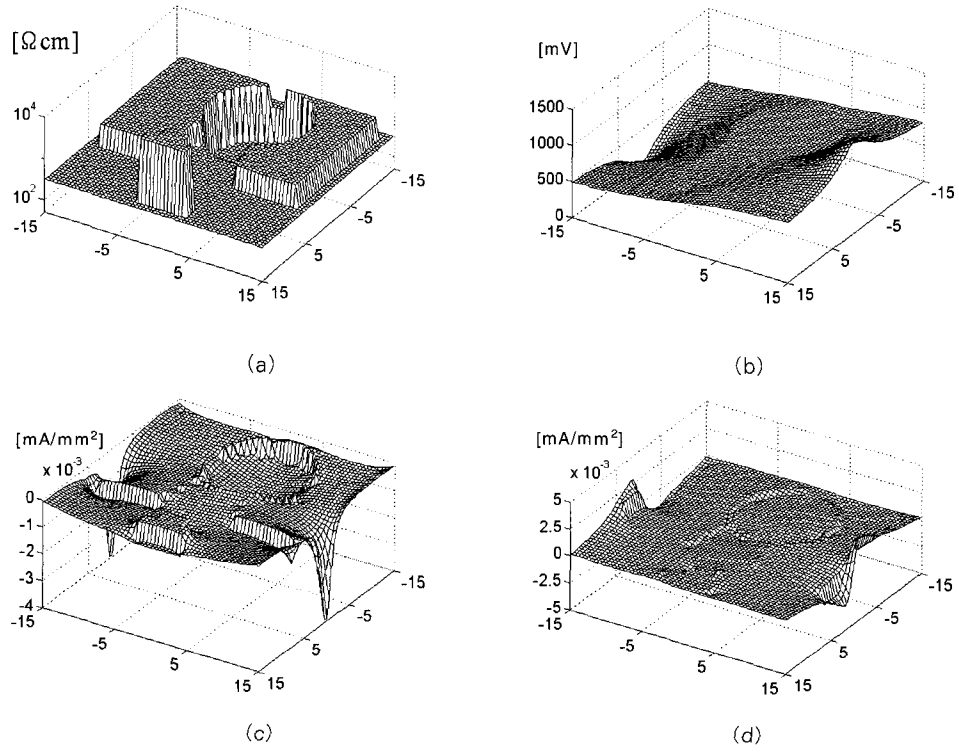

Fig. 7. (a) Resistivity distribution on the xy-plane with $z = 0$ mm of the thorax model in Fig. 2(c). Computed (b) V, (c) J_x, and (d) J_y on the same plane.

and B_y are relative small compared to B_z only when the current density distributions are symmetric along z-direction with respect to the plane we compute the magnetic flux density. Fig. 9(e), (f), and (g) show the computed J_x^B, J_y^B, and J_z^B, respectively. We can see that J_z^B is no longer negligible since there must exist current densities out of the plane. Fig. 9(h) shows the vector plot of J^B on the same plane. The compatibility condition and continuity equations are also all satisfied with negligibly small rms errors in this plane.

DISCUSSION

For the computation of $B(r)$ with $r \in \Omega$ in (3), we must include the effect of lead wires. As shown in the previous section, we found that both analytic formula and single-line FEM methods provide wrong numerical results of $B(r)$ in Ω. We believe that these two methods fail without properly handling the singularity at two nodal points of $r=(0, \pm L, 0)$. However, using more sophisticated electrode models including the conditions in (8), these methods may be able to pass the compatibility tests.

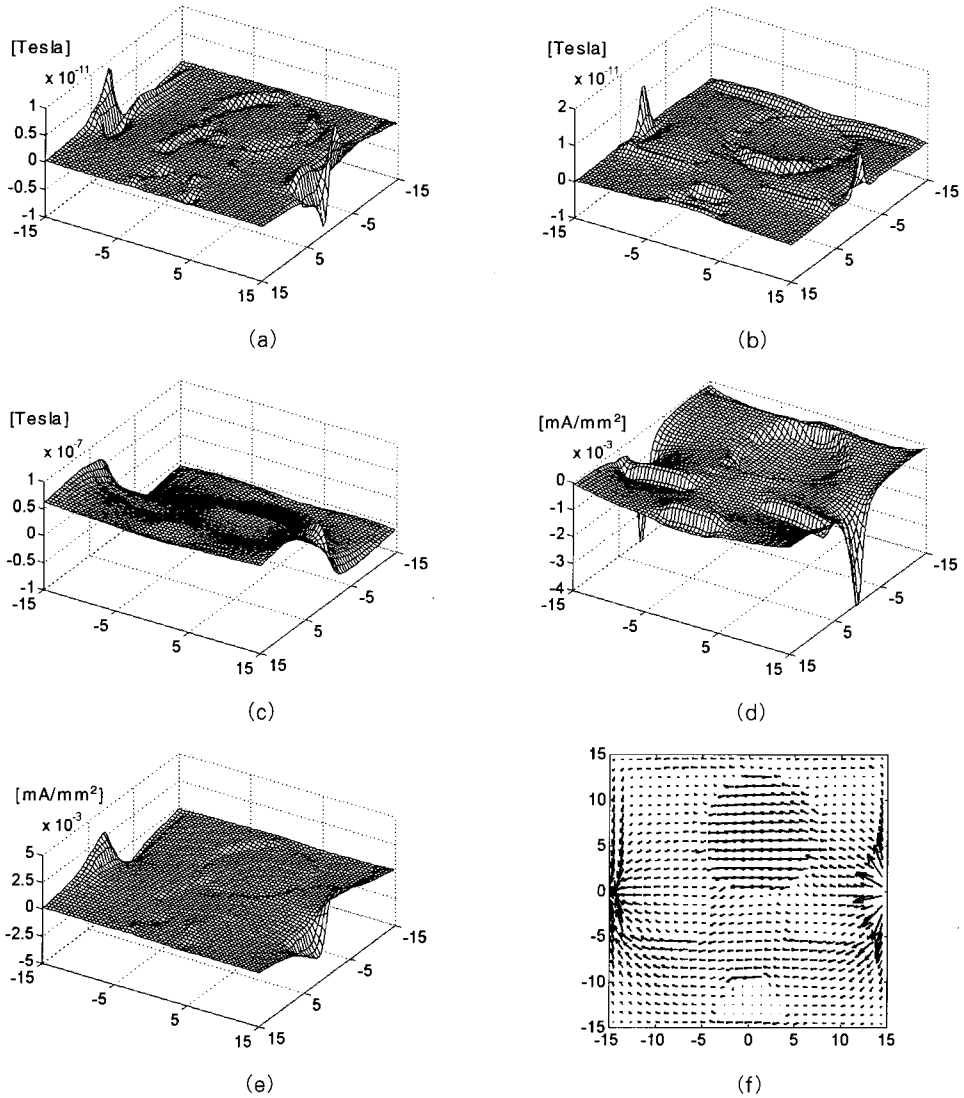

Fig. 8. Computed (a) B_x, (b) B_y, and (c) B_z on the xy-plane with z = 0 mm in Ω for the thorax model shown in Fig. 2(c). Computed (d) J_x^B and (e) J_y^B on the same plane. (f) Vector plot of J^B on the same plane.

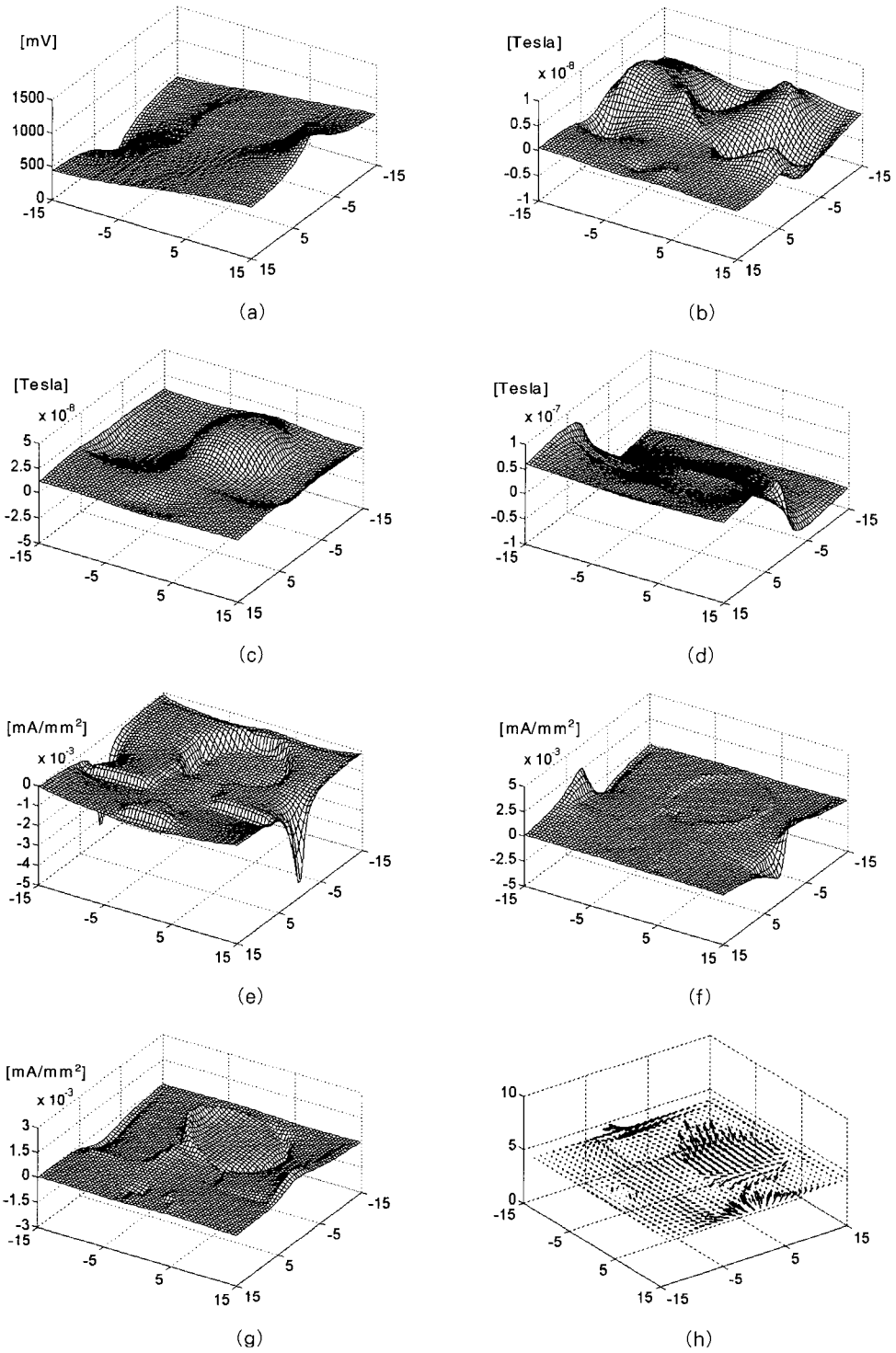

Fig. 9. Computed (a) V, (b) B_x, (c) B_y, and (d) B_z on the xy-plane with z = 42.85 mm in Ω for the thorax model shown in Fig. 2(c). Computed (e) J_x^B, (f) J_y^B, and (g) J_z^B on the same plane. (h) Vector plot of J^B on the same plane.

As described in the previous section, the multi-line FEM method in computing $B(r)$ in (3) provides correct numerical results though it requires much more amount of computations. In [14], we showed that it is possible to

significantly reduce the amount of computations by adopting an analytical integration formula in x- and y-direction.

For the injection current of 55 mA, we found that B_z is in the order of 10^{-7} Tesla. Depending on the resistivity distribution and the xy-plane where we compute, the magnetic flux density, we found that B_x and B_y are in the range of 10^{-11} to 10^{-8} Tesla. As described in [13, 19], even though we can measure the magnetic flux density in this range using a 0.3 Tesla MRCDI system, the *SNR* is relatively low. Since we need to differentiate $B(r)$ to obtain $J(r)$ as in (7), we want a higher *SNR* in the measurements of $B(r)$. Furthermore, we must reduce the amount of injection current to less than 5 mA when we apply this technique to a human subject. This means that we should use an MRCDI system based on an MRI system with much higher (at least 1.5 Tesla) main magnetic field intensity. We will utilize the numerical analysis methods described in this paper to derive the requirements of an MRCDI system to obtain reliable magnetic flux density data.

In the conventional MRCDI technique, we can measure only one component of $B(r)$ since MR phase images contain the information on the component of $B(r)$ that is parallel to the main magnetic field of the MRI system. This means that we must rotate the subject in order to acquire all three components of $B(r)$ as is done in [13]. The numerical results in the previous section indicate that B_z is always larger than B_x and B_y. Therefore, we are developing a new MRCDI technique where we can reconstruct a current density distribution based on the measurement of only B_z in multiple slices along z-direction.

CONCLUSION

In this paper, we described the three-dimensional numerical analysis method in MRCDI. We found that it is critical to correctly handle the singularity problem near electrodes in computing the internal magnetic flux density due to an injection current. Using the method described in this paper, the computed magnetic flux density contains an error vector that is curl and divergence free. However, the computed current density from the magnetic flux density should contain no other error except numerical errors. Therefore, this method is sufficient for MRCDI.

The numerical analysis method described in this paper will be used in our future studies including the design of MRCDI procedure and verification of experimental results. The numerical analysis of MRCDI technique provides us much insight to devise a new innovative method of internal current density imaging without subject rotation. We plan to focus our research efforts in mathematical analysis and experimental verification of this new technique. Internal current density imaging without subject rotation will be a valuable tool in functional imaging such as MREIT. We speculate that it may also provide new diagnostic information on internal temperature, ion concentration, tissue composition, and others.

REFERENCES

1. M.L.G. Joy, G.C. Scott, and R.M. Henkelman, "*In vivo detection of applied electric currents by magnetic resonance imaging,*" *Mag. Reson. Imag.*, vol. 7, pp. 89-94, 1989
2. G.C. Scott, M.L.G. Joy, R.L. Armstrong, and R.M. Henkelman, "*Measurement of nonuniform current density by magnetic resonance,*" *IEEE Trans. Med. Imag.*, vol. 10, no. 3, pp. 362-374, 1991
3. G.C. Scott, M.L.G. Joy, R.L. Armstrong, and R.M. Henkelman, "*Sensitivity of magnetic-resonance current density imaging,*" *J. Mag. Res.*, vol. 97, pp. 235-254, 1992
4. M. Eyuboglu, R. Reddy, and J.S. Leigh, "*Imaging electrical current density using nuclear magnetic resonance,*" *Elektrik*, vol. 6, no. 3, pp. 201-214, 1998
5. G.C. Scott, M.L.G. Joy, R.L. Armstrong, and R.M. Henkelman, "*Eletromagnetic considerations for RF current density imaging,*" *IEEE. Trans. Med. Imaging*, vol. 14, no. 3, pp. 515-524, 1995
6. H.R. Gamba and D.T. Delpy, "*Measurement of electrical current density distribution within the tissues of the head by magnetic resonance imaging,*" *Med. Biol. Eng. Comp.*, vol. 36, pp. 165-170, 1998
7. M.L.G. Joy, V.P. Lebedev, and J.S. Gati, "*Imaging of current density and current pathways in rabbit brain during transcranial electrostimulation,*" *IEEE Trans. Biomed. Eng.*, vol. 46, no. 9, pp. 1139-1149, 1999
8. E.J. Woo, S.Y. Lee, and C.W. Mun, "*Impedance tomography using internal current density distribution measured by nuclear magnetic resonance,*" *SPIE*, vol. 2299, pp. 377-385, 1994
9. O. Kwon, J.K. Seo, E.J. Woo, and J.R. Yoon, "*Magnetic resonance electrical impedance tomography,*" *Comm. Korean Math. Soc.*, vol. 16, no. 3, pp. 519-541, 2000

10. M. Eyuboglu, O. Birgul, and Y.Z. Ider, "*A dual modality system for high resolution-true conductivity imaging,*" *Proc. XI Int. Conf. Elec. Bioimpedance (ICEBI)*, pp. 409-413, 2001
11. Birgll, O. zbekl, B.M. Eyboglul, Y.Z. Ider, "*Magnetic resonance conductivity imaging using 0.15 Tesla MRI scanner,*" *Proc. 23rd. Ann. Int. Conf. IEEE Eng. Med. Biol. Soc.*, 2001
12. O. Kwon, E.J. Woo, J.R. Yoon, and J.K. Seo, "*Magnetic resonance electrical impedance tomography (MREIT): simulation study of J-substitution algorithm,*" *IEEE Trans. Biomed. Eng.*, vol. 48, no. 2, pp. 160-167, 2002
13. H.S. Khang, B.I. Lee, S.H. Oh, E.J. Woo, S.Y. Lee, M.H. Cho, O. Kwon, J.R. Yoon, and J.K. Seo, "*J-substitution algorithm in magnetic resonance electrical impedance tomography (MREIT): phantom experiments for static resistivity images,*" *IEEE Trans. Med. Imaging*, vol. 21, no. 6, pp.695-702, 2002
14. B.I. Lee, S.H. Oh, E.J. Woo, S.Y. Lee, M.H. Cho, O. Kwon, J.R. Yoon, and J.K. Seo, "*Three-dimensional forward solver for magnetic resonance electrical impedance tomography(MREIT),*" submitted to *IEEE Trans. Biomed. Eng.*, 2002
15. D.K. Cheng, *Field and Wave Electromagnetics*, 2nd. ed., Reading, MA, Addison-Wesley, 1989
16. J. Jin, *The Finite Element Method in Electromagnetics*, New York, NY, John Wiley & Sons, 1993
17. D.S. Burnett, Finite *Element Analysis*, Reading, MA, Addison-Wesley, 1987
18. J.R Yoon, "*Calculation of B including lead-wire effects,*" KHU Internal Document, 2001
19. S.H. Oh, B.I. Lee, E.J. Woo, S.Y. Lee, M.H. Cho, O. Kwon, J.R. Yoon, and J.K. Seo, "*Magnetic resonance current density imaging for MREIT,*" submitted to *J. Biomed. Eng. Research*, 2002